

Simulation of ultrasonic phased array technique for imaging and sizing of defects using longitudinal waves

L. Satyanarayan, C. Sridhar, C.V. Krishnamurthy, Krishnan Balasubramaniam*

Center for Non-Destructive Evaluation and Department of Mechanical Engineering, Indian Institute of Technology Madras, Chennai 600 036, India

Received 3 October 2006; received in revised form 26 June 2007; accepted 1 August 2007

Abstract

Phased array ultrasonics can be used as a rapid tool for imaging and sizing crack-like defects. This paper reports the simulation of phased array ultrasonic wave interaction with the defects using the finite-difference time domain (FDTD) method. Experiments were conducted to validate modeling results for pulse–echo simulations of the phased array transducer on a mild-steel (MS) pipe sample with circumferential internal surface notches of three different sizes. Experiments were carried out on the MS pipe specimen using a conventional ultrasonic technique with a 5 MHz transducer at 45° refracted angle within the specimen and the defects were imaged and sized using the relative arrival time technique (RATT). The experimental B-scans obtained using the conventional ultrasonic techniques were compared with the experimental B-scans obtained using the phased array instrument. Simulation studies were also carried out by steering the beam to the requisite angles by the phased array transducer to study the effect of various angles of incidence on the defect definition, i.e., with respect to imaging and sizing, using the RATT.

© 2007 Elsevier Ltd. All rights reserved.

Keywords: Crack sizing; Ultrasonic phased array; Circumferential surface cracks; FDTD; RATT

1. Introduction

Ascertaining the structural integrity of critical engineering components such as pressure vessels [1,2] is an important requirement and also calls for a reliable and fast non-destructive evaluation technique, especially under field conditions [3]. Eddy current-based techniques [4] are widely used for the detection and characterization of surface and near-surface cracks in conductive materials. It is based on the principle of electromagnetic induction and essentially involves the measurement of the impedance at every point on the scan surface. A change in the impedance is observed if a crack is present, which is taken as an indication for the detection and sizing of the defect. Infrared thermography is based on the measurement of infrared energy (active/passive) emitted from the component and is displayed as the temperature distribution within the body. Defects in the components become clearly visible

as the temperature gradient between a defective and a non-defective region is distinctly high [5]. The acoustic emission technique [6] has been extensively used for the condition monitoring of engineering components. Transducers are attached on the components under study to pick up stress signals in the form of elastic waves when a crack develops or propagates, which is often associated with the release of energy. A number of appropriately placed sensors are used to accurately detect and position the defects. This technique has been used to study fatigue crack propagation in various power plant components. Traditional ultrasonics is a very common and reliable technique that is used for the detection of defects in components. It is based on the principle that when ultrasonic energy is incident on a defect, the surface of the defect reflects the energy at an angle dictated by the laws of reflection. The reflected signal is picked up and the amplitude of the reflected signal gives an indication of the size of the defect. Advanced ultrasonic methods like the time of flight diffraction (TOFD) technique [7], synthetic aperture focusing technique (SAFT) [8] and phased array techniques [9,10] have been

*Corresponding author. Tel.: +91 44 2257 4662; fax: +91 44 2257 0545.
E-mail address: balas@iitm.ac.in (K. Balasubramaniam).

Nomenclature

c	longitudinal wave velocity
C_{ijkl}	elastic stiffness tensor
E	Young's modulus
f	frequency
G	shear modulus
u	velocity along x -direction
t	time
v	velocity along y -direction
x, y	Cartesian directions
Z	acoustic impedance

t_n	required time delay to the n th element
N	total number of active elements
n	element number (0,1,2,...,N-1)
d	center-to-center spacing between the elements
F	depth of focus
α	attenuation factor
λ, μ	Lame's constants
τ_{xx}, τ_{zz}	normal stress
τ_{xz}	shear stress
ν	Poisson's ratio
θ	angle of incidence or steer
ρ	density

also been extensively used to accurately detect and size cracks in critical engineering components.

Phased array ultrasound has emerged as a rapid non-destructive evaluation technique for the detection and imaging of crack-like defects in structural components due to the flexibility it offers in varying the angle of inspection and/or focusing of the beam to a point of interest [11–14]. The principle of phased array ultrasonic beam generation is based on the use of individual transducer elements that can each be independently driven with controlled phase delays of excitation. Using this phase delay, the parameters of the ultrasonic beam, such as the depth of focus and/or the beam angle can be varied while the testing is being carried out. This results in an improved capability to image defects located in regions even with limited accessibility. Using the linear scanning capability of the phased array, the manual/automated motion of the ultrasonic probe during flaw detection is replaced by the near-real-time electronic scanning. Fig. 1(a) shows how a beam can be steered at an angle in a specimen with a crack-like defect that is computed using the finite-difference time domain (FDTD) method [15].

Conducting the experiments over a wide range of defects and specimen geometries is both time consuming and costly. The high cost of a phased array transducer is also a factor that motivates the use of models for simulation of the experimental procedures. In such cases, numerical methods such as the FDTD method can be suitably used to solve for the displacement and stress values in the domain of interest. The simulation results may be utilized in the design of experiments, optimal selection of experimental parameters such as the transducer frequency, depth of focus, angle of inspection, determination of focal laws and the interpretation of defect images. Fig. 1(b) shows the interaction of a phase steered wave at different instances of its propagation with a bottom surface crack simulated by the FDTD method. The corner trap and the tip diffracted echoes are clearly seen.

In this paper, simulation of the phased array ultrasound wave propagation in a 10-mm thick mild-steel (MS) pipe specimen with circumferential internal surface notches has

been demonstrated using the FDTD method. The simulations of B-scans were compared with the corresponding experimentally obtained B-scans using the phased array instrument.

The effect of varying angles of incidence on the definition, ease and accuracy of sizing of the defects using the relative arrival time technique (RATT) was also explored by changing the refracted angles within the specimen by the phased array transducer. The study also investigates the effect of the inclination of a bottom surface crack on its image obtained using the RATT.

2. Finite-difference time domain formulation of the problem

The FDTD model for the simulation and visualization of the elastic wave propagation is based on a first-order velocity–stress finite-difference method for homogeneous isotropic material [16]. The equation of motion, the stress–strain relation together with constitutive equations, completely describes the elastic wave propagation in a homogenous material.

In the elastic media, the relationship between stresses and strains can be written as

$$\tau_{ij} = c_{ijkl} u_{k,l}, \quad (1)$$

where the summation convention has been implied.

The c_{ijkl} term is a matrix of the order 6×6 and contains 36 elastic moduli. For an isotropic case, the number of elastic moduli reduces to only 2, and can be written in terms of Lamé's constants, λ and μ .

The derivative of Eq. (1) with respect to the time variable can be written as

$$\tau_{ij}^\circ = c_{ijkl} v_{k,l}, \quad (2)$$

where v is the velocity and based on Newton's law

$$\rho v_i = \tau_{ij,j}. \quad (3)$$

The above equation leads to a set of first-order partial differential equations that are coupled. The elastic wave

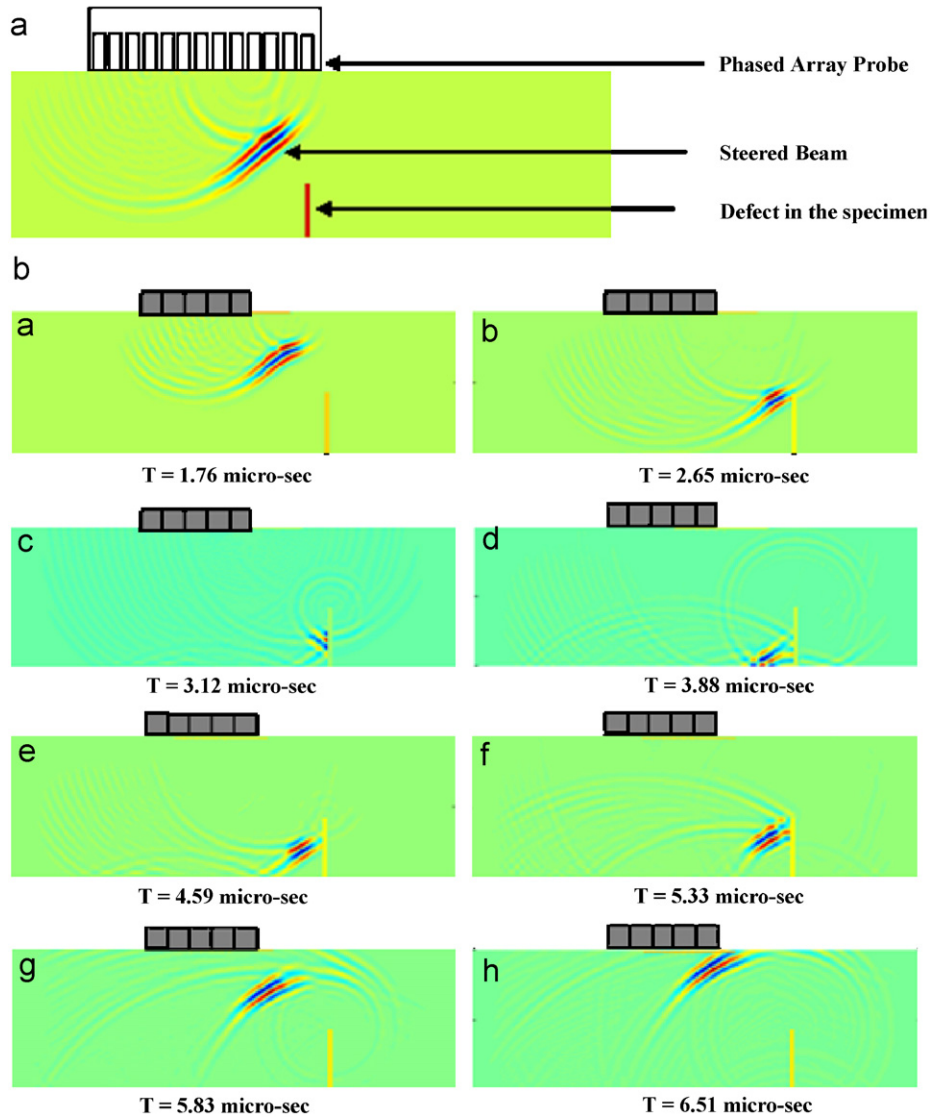


Fig. 1. (a) Beam steering and focusing in a phased array transducer. (b) Interaction of a phase steered wave with the crack tip and corner.

equation in two dimensions are given by

$$\rho \frac{\partial v_x}{\partial t} = \frac{\partial \tau_{xx}}{\partial x} + \frac{\partial \tau_{xz}}{\partial z},$$

$$\rho \frac{\partial v_z}{\partial t} = \frac{\partial \tau_{xz}}{\partial x} + \frac{\partial \tau_{zz}}{\partial z},$$

$$\frac{\partial \tau_{xx}}{\partial t} = (\lambda + 2\mu) \frac{\partial v_x}{\partial x} + \lambda \frac{\partial v_z}{\partial z}, \quad (4)$$

$$\frac{\partial \tau_{zz}}{\partial t} = (\lambda + 2\mu) \frac{\partial v_z}{\partial z} + \lambda \frac{\partial v_x}{\partial x}, \quad (5)$$

$$\frac{\partial \tau_{xz}}{\partial t} = \lambda \left(\frac{\partial v_x}{\partial z} + \frac{\partial v_z}{\partial x} \right). \quad (6)$$

The differential equations are discretized by the finite-difference scheme, which are obtained by truncating Taylor

series expansion. This may lead to numerical errors that cannot be avoided. The choice of programming scheme and the parameters must be so chosen that numerical error and instability do not diversify at any point in the wave propagation. The finite-difference discretization of the set of equations leads to a staggered finite-difference grid as shown in Fig. 2. Here the normal stresses, namely τ_{xx} and τ_{zz} , are represented at a single node and the remaining field (velocity) variables, v_z and v_x , and the shear component τ_{xz} are represented in the grid at half-spatial steps to each other.

The velocity and the stress components in the grid are not known at the same position in time and space and are offset by $\Delta t/2$ and $\Delta x/2$, $\Delta y/2$ as shown in the Fig. 2. This leads to a leap frog scheme in which the velocity components are updated at the $(\Delta t/2)$ first half-time step and then in the next half-time step, stress components are

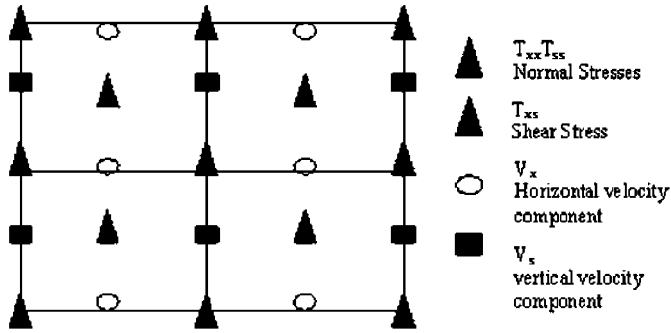


Fig. 2. Finite difference grid of the domain showing the positions of each field variable.

updated. In the next $\Delta t/2$, with the stress components at the end of the first time step, Δt , the velocity components at $(\Delta t + \Delta t/2)$ are calculated.

The velocity components u and v are determined from Eq. (1):

$$\begin{aligned} \rho \frac{u_{ij}^{k+1} - u_{ij}^{k-1}}{\Delta t} &= \left[\frac{(\tau_{xx})_{i+1,j}^k - (\tau_{xx})_{i-1,j}^k}{\Delta x} \right] \\ &+ \left[\frac{(\tau_{xz})_{i,j+1}^k - (\tau_{xz})_{i,j-1}^k}{\Delta z} \right], \\ u_{ij}^{k+1} &= u_{ij}^{k-1} + \left[\frac{(\tau_{xx})_{i+1,j}^k - (\tau_{xx})_{i-1,j}^k}{\rho \Delta x / \Delta t} \right] \\ &+ \left[\frac{(\tau_{xz})_{i,j+1}^k - (\tau_{xz})_{i,j-1}^k}{\rho \Delta z / \Delta t} \right], \end{aligned} \quad (7)$$

$$\begin{aligned} \rho \frac{v_{ij}^{k+1} - v_{ij}^{k-1}}{\Delta t} &= \left[\frac{(\tau_{xz})_{i+1,j}^k - (\tau_{xz})_{i-1,j}^k}{\Delta x} \right] \\ &+ \left[\frac{(\tau_{yy})_{i,j+1}^k - (\tau_{yy})_{i,j-1}^k}{\Delta z} \right], \\ v_{ij}^{k+1} &= v_{ij}^{k-1} + \left[\frac{(\tau_{xz})_{i+1,j}^k - (\tau_{xz})_{i-1,j}^k}{\rho \Delta x / \Delta t} \right] \\ &+ \left[\frac{(\tau_{yy})_{i,j+1}^k - (\tau_{yy})_{i,j-1}^k}{\rho \Delta z / \Delta t} \right]. \end{aligned} \quad (8)$$

The stress components (two normal components and one shear component) are determined by

$$\begin{aligned} \frac{(\tau_{xx})_{ij}^{k+1} - (\tau_{xx})_{ij}^{k-1}}{\Delta t} &= \left[\frac{(\lambda + 2\mu)(u_{i+1,j} - u_{i-1,j})}{\Delta x} \right] \\ &+ \left[\frac{\mu(v_{i,j+1} - v_{i,j-1})}{\Delta z} \right], \\ (\tau_{xx})_{ij}^{k+1} &= (\tau_{xx})_{ij}^{k-1} + \left[\frac{(\lambda + 2\mu)(u_{i+1,j} - u_{i-1,j})}{\Delta x / \Delta t} \right] \\ &+ \left[\frac{\mu(v_{i,j+1} - v_{i,j-1})}{\Delta z / \Delta t} \right], \end{aligned} \quad (9)$$

$$\begin{aligned} \frac{(\tau_{zz})_{ij}^{k+1} - (\tau_{zz})_{ij}^{k-1}}{\Delta t} &= \left[\frac{(\lambda + 2\mu)(v_{i+1,j} - v_{i-1,j})}{\Delta x} \right] \\ &+ \left[\frac{\lambda(u_{i,j+1} - u_{i,j-1})}{\Delta z} \right], \\ (\tau_{zz})_{ij}^{k+1} &= (\tau_{zz})_{ij}^{k-1} + \left[\frac{(\lambda + 2\mu)(v_{i+1,j} - v_{i-1,j})}{\Delta x / \Delta t} \right] \\ &+ \left[\frac{\lambda(u_{i,j+1} - u_{i,j-1})}{\Delta z / \Delta t} \right], \end{aligned} \quad (10)$$

$$\begin{aligned} \frac{(\tau_{xz})_{ij}^{k+1} - (\tau_{xz})_{ij}^{k-1}}{\Delta t} &= \left[\frac{(\lambda)(v_{i+1,j} - v_{i-1,j})}{\Delta x} \right] \\ &+ \left[\frac{\lambda(u_{i,j+1} - u_{i,j-1})}{\Delta z} \right], \\ (\tau_{xz})_{ij}^{k+1} &= (\tau_{xz})_{ij}^{k-1} + \left[\frac{\lambda(v_{i+1,j} - v_{i-1,j})}{\Delta x / \Delta t} \right] + \left[\frac{\lambda(u_{i,j+1} - u_{i,j-1})}{\Delta z / \Delta t} \right]. \end{aligned} \quad (11)$$

Courant number is the ratio of the distance the elastic wave travels in one time step to the length of a step of the mesh. In order to ensure stability and obtain numerical convergence in the FDTD method, it is essential that the Courant number is less than or equal to one. Hence, in the simulations, stability criteria of Courant number ($c\Delta t/\Delta x$) lesser than one are always considered.

Appropriate boundary conditions need to be applied while implementing the FDTD technique to define the defect and the specimen boundaries. A variety of techniques are available to apply a free boundary condition for staggered grid FDTD schemes. In this study, the velocities along the back wall and the defect boundaries were set to zero [17], i.e., $u = 0$; $v = 0$.

During modeling, in order to reduce the computational resource requirements a sub-domain region of the specimen is used. This domain process creates artificial free boundaries that lead to undesirable reflections and mode conversions that do not occur in the experiments. In order to eliminate these artifact reflected waves, the absorbing boundary conditions were applied on the appropriate domain boundaries. The absorbing boundary conditions can be implemented by incorporating the perfectly matching layer (PML) boundary conditions [18]. Perfectly matching layers are an extra set of layers that are incorporated outside the domain of the model whose impedance and phase velocity match with that of the domain and also have an attenuation function that rapidly decays the wave that proceeds through the layers. Since there is no impedance mismatch between the perfectly matching layer and the domain, very little reflection occurs at the domain–perfectly matching layer boundary.

However, in discrete space, the lossy layer will not be perfectly matched to the solution space domain and slight reflections occur at the interface. In order to minimize these reflections, a tapered loss profile function was chosen within the lossy layers

$$\alpha_i = \alpha_{\max}[(i - i_{\text{pml}})/N_{\text{pml}}]^2, \quad (12)$$

where N_{pml} is the thickness of the perfectly matching layers in terms of the number of cells and $i - i_{\text{pml}}$ is the position in the perfectly matching layers.

3. Phased array ultrasonic system

The experimental setup used in this study consists of a commercial ultrasonic phased array system with the array probe using the electronic scanning feature on the MS pipe specimen. The data presented in this paper were acquired using 5 MHz center frequency and a 64-element (46 mm × 15 mm area) array probe. The defects were imaged by phasing the elements of the probe to generate a longitudinal wave steered at the requisite angle of inspection in the linear scan mode.

4. Simulation of A-scan signals and B-scan images using finite-difference time domain technique

A two-dimensional (2D) model was developed using the FDTD technique to simulate the phased array wave propagation in rectangular block and pipe-like structures. The density of the MS pipe was taken as 7900 kg/m³ and the longitudinal wave velocity was assumed to be 5900 m/s while the shear wave velocity was assumed to be 3200 m/s. The defects simulated in the pipe sample were surface notches from the inner diameter (ID) of three different sizes.

The 2D model was developed in MATLAB[®] to simulate the propagation of the ultrasonic wave in the specimen of an arbitrary geometry. The 2D plane of the pipe was in the $r-z$ direction and hence can be approximated as a plate using the plane wave assumption. The simulated cracks were modeled to be oriented in the $r-\theta$ plane. The code takes input parameters that define a phased array experimental setup and generates A-scans and B-scans that can be compared with the corresponding experimental A-scans and B-scans. The time delay/focal laws [19] given in Eq. (14) have been used to simulate phased array transmission and reception of unfocused phase steered beams. Fig. 3 shows the finite-difference model of the specimen along with the transmission and reception delay scheme applied to simulate the phased array transducer. In order to replicate the experimental conditions, the number of elements in the simulation that have been kept active was 16 for all scans and the beam was steered at 45° to the normal with respect to the center of the probe from an ultrasonic phased array transducer of 5 MHz center frequency. A three-cycle Hanning window pulse was chosen as input to the transducer elements for the simulations. The elements of the transducer (assumed to be point sources) generates spherical wave fronts which interfere constructively as dictated by the phase delay laws and get steered at the required angle of inspection. The grid size in the model was

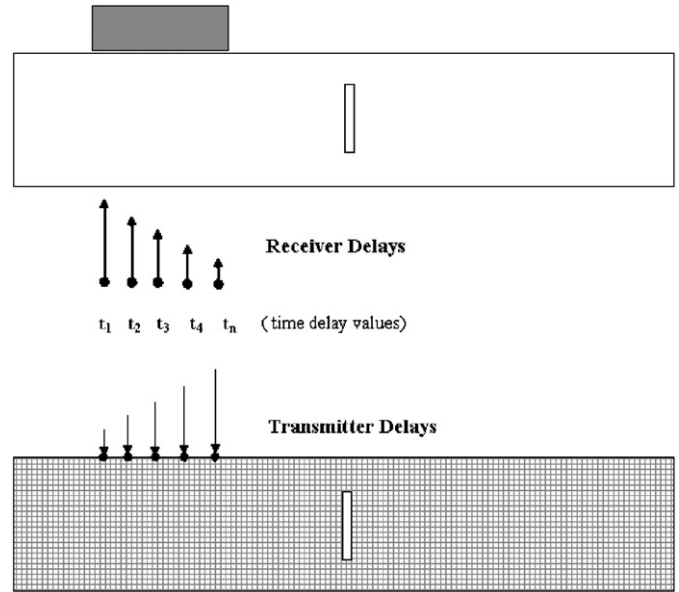


Fig. 3. Finite difference model for phased array transmission and reception.

Table 1
Settings used in the simulation study

Transducer specifications	
Central frequency	5 MHz
Transducer length	46 mm
Transducer width	15 mm
Type of wave used	Longitudinal
Inspection angle	45°
Discretization parameters	
Time step size	9.43e−9 s
Element size	8.4e−002 mm ($\lambda/15$)
Material properties (mild steel)	
L-wave velocity	5900 m/s
S-wave velocity	3200 m/s
Density	7900 kg/m ³

taken as (wavelength) $\lambda/15$.

$$t_n = (F/c) \{ [1 + (((N-1)/2)(d/F))^2 + (2((N-1)/2)d \sin \theta/F)]^{(1/2)} - [1 + ((n - ((N-1)/2 - 1)*d/F))^2 - 2(n - ((N-1)/2)d \sin \theta/F)]^{(1/2)} \}. \quad (13)$$

If the beam is unfocused, the above expression for the time delay to the n th element reduces to

$$t_{n(\text{transmit})} = [nd \sin \theta/c] \quad \text{during transmission}, \quad (14)$$

$$t_{n(\text{receive})} = [(N-n)d \sin \theta/c] \quad \text{during reception}. \quad (15)$$

During transmission, the nodes that represent the active transducer elements were provided displacements at time delay values given by the well-known transmit delay law provided in Eq. (14). Using these time delays, the wave was

steered at the requisite angle within the specimen. The received signals are then time-advanced using the reception delay law and then summed together to generate the A-scan at that inspection point. The defects in the specimen are modeled as free surfaces which reflect/diffract the entire acoustic energy incident on them. Once a wave meets an interface, new reflected waves are created based on the angle of incidence taking into account mode conversion. This model does not account for attenuation the wave undergoes as it travels in the specimen. The internal reflection within the transducer, which accounts for the noise near the front wall region, has also not been modeled. The settings that have been used for the simulation study are given in Table 1.

5. Experimental results

5.1. Imaging and sizing of circumferential bottom surface notches in pipes

Experiments were conducted on a 10-mm thick MS pipe sample with 3-, 5- and 7-mm deep (i.e., 30%, 50% and 70% of the pipe thickness) vertical electrical discharge machined surface notches using phase steered 45° longitudinal wave using 64-element phased array transducer of 5 MHz center frequency. The MS pipe sample is shown in Fig. 4. The details of electrical discharge machined notches with respect to the vertical of a 10-mm thick MS pipe sample are given in Table 2.

Fig. 5(a) shows the schematic representation of the ultrasound ray path between crack tip and corner trap signal for an internal surface breaking crack. The size of the defect was then determined by time of flight technique by reading the A-Scans obtained from the B-scan data. A rectified A-scan with two distinct echo signals from the crack is shown in Fig. 5(b). The echo of smaller amplitude is from the crack tip and the echo of higher amplitude corresponds to the reflection from the corner trap. The crack height at that point can be estimated from the A-scan signal by measuring the relative time difference between the two echo peaks taking into consideration the angle of incidence and the material properties. An alternate method involves the analysis of the B-scan image and measuring the relative displacement of the probe position (at the maximum height of the signals) as an indication of the size

of the defect. In case of a 45° LW inspection, the size of the defect is equal to the displacement of the probe between the maximum positions of the tip diffracted and the corner trap echo peaks. Since, in the electronic scanning feature of the phased array, the resolution of the alternate technique is limited by the inter-element spacing, the RATT method has been employed to size the defect.

Fig. 5(c) shows a B-scan image of a 5-mm deep bottom surface notch in a 10-mm deep MS pipe specimen. The 45° phase steered beam first interacts with the top tip of the defect and is diffracted, which is seen as the first echo in the image. The compressional/longitudinal wave then hits the defect corner and gets mode converted into a compressional/longitudinal component (P–P wave) and a shear component (P–S wave). Since the velocity of the P-wave is higher, it arrives earlier when compared with the S-wave in the B-scan image.

Fig. 6(a)–(c) shows a comparison of experimental and simulated B-scans for a pipe with notches of three different sizes present on the inner diameter. The notches were sized using the RATT [20–23]. The estimated sizes of the defects and the associated percentage errors are given in Table 3. It was observed that the simulated results were in good agreement with the experimental results.

5.2. Effect of varying angles of inspection in relative arrival time technique on imaging of circumferential bottom surface notches in pipes

The RATT method involves the measurement of the corner trap and the top tip diffracted echoes by the same angle for the estimation of the size of the crack. If the relative ultrasound path between the corner trap and

Table 2

Details of circumferential EDM notches with respect to vertical of 10-mm thick mild-steel pipe sample

Defect number	Type	Length (mm)	Width (mm)	Depth (mm)
D1	Internal surface breaking (rectangular)	10	0.4	7
D2	Internal surface breaking (rectangular)	10	0.4	5
D3	Internal surface breaking (rectangular)	10	0.4	3

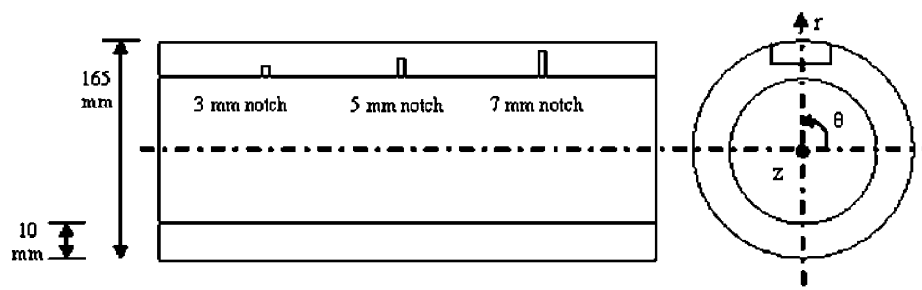


Fig. 4. Line sketch of 10-mm thick mild-steel pipe sample with three inner diameter notches in the circumferential direction.

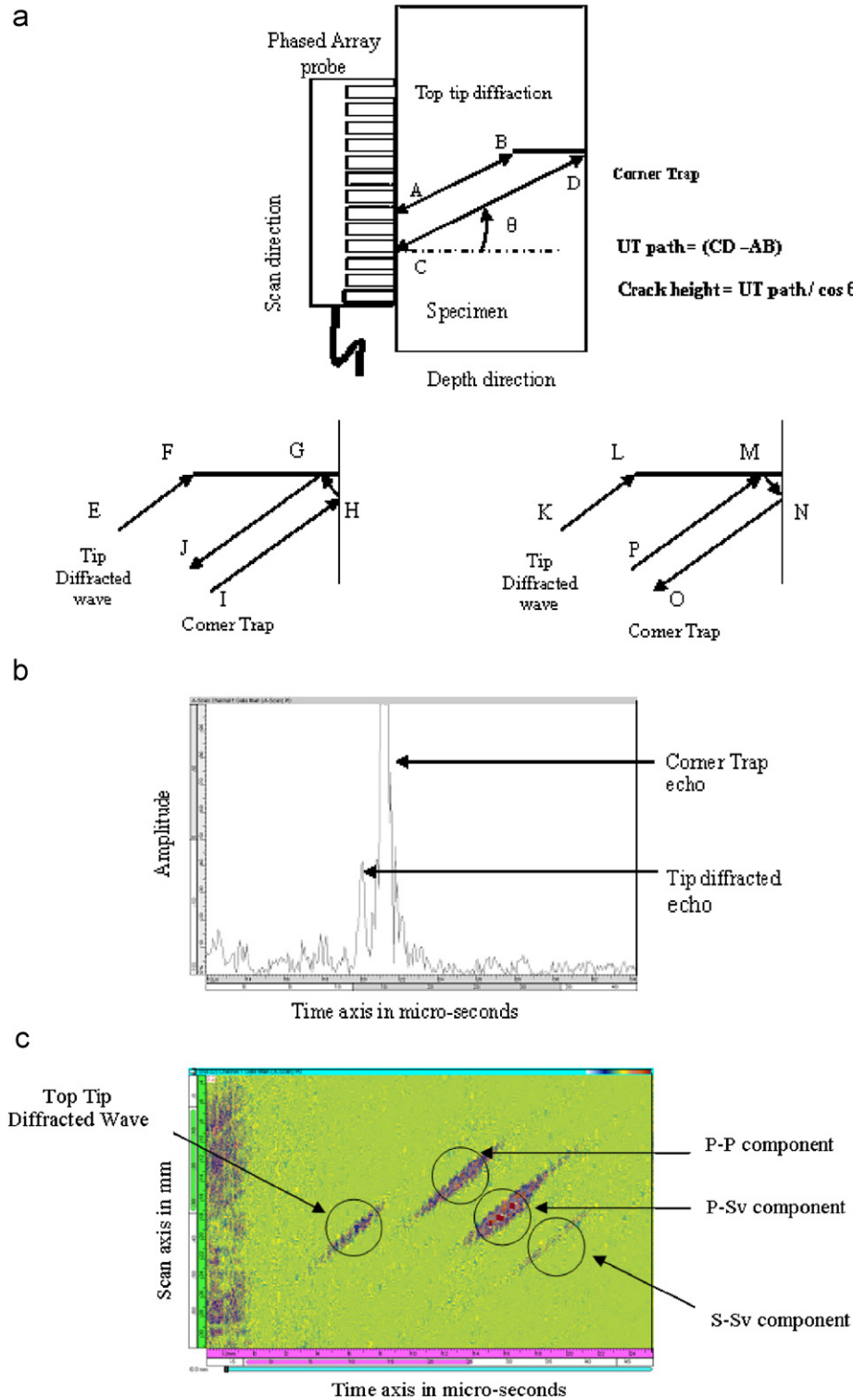


Fig. 5. (a) Ultrasound path between crack tip and corner trap signal for a surface crack. (b) A-scan showing crack tip and corner trap echo signal for a surface crack. (c) Experimental B-scan image of a 5-mm bottom surface notch.

the top tip diffracted echo is “ UT_{path} ”, then

$$H = UT_{\text{path}} / \cos \theta, \quad (16)$$

where H = crack height and θ = angle of inspection.

$$UT_{\text{path}} = (\overline{CD} - \overline{AB}).$$

The angle of inspection is inbuilt in the estimation of the size of the crack, which automatically compensates for the change in the ultrasound path due to the change in the inspection angle. But, the determination of an optimum inspection angle is desirable for a clear image of the defect signals in the B-scan. Thus, the defects were imaged using

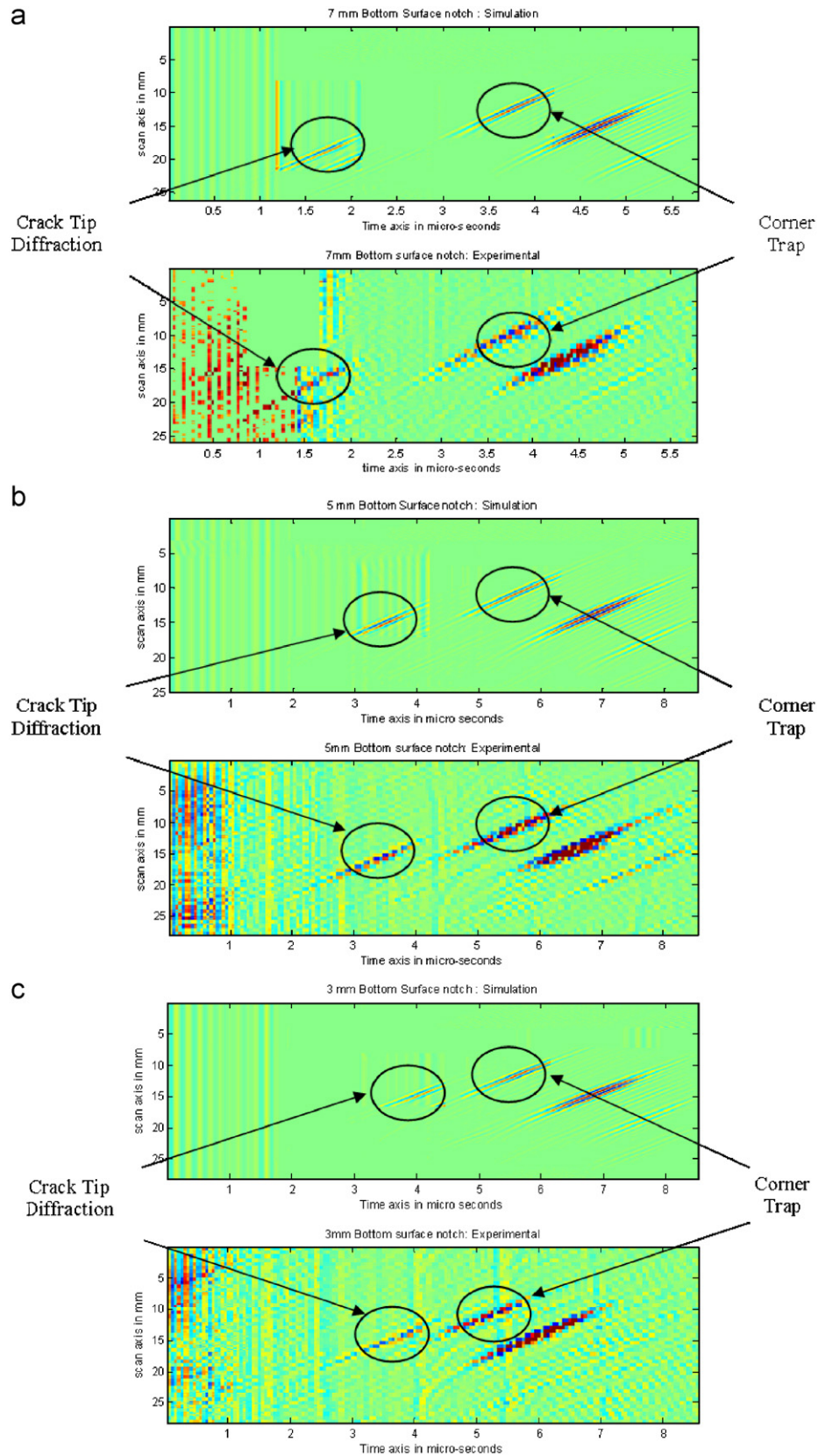


Fig. 6. Comparison of simulated and experimental B-scan images on a 10-mm thick mild-steel pipe sample with bottom surface notches. (a) 7-mm, (b) 5-mm and (c) 3-mm bottom surface notches.

Table 3

Comparison of the simulated and experimental estimated notch sizes obtained by relative arrival time technique on 10-mm thick mild-steel pipe sample at 45° angle of incidence

Defect number	Actual depth (mm)	Estimated depth (mm): simulated	Percentage error: simulated	Estimated depth (mm): experimental	Percentage error: experimental
D1	7	7.2	−2.85	7.4	−5.71
D2	5	4.8	+4.0	4.7	+5.99
D3	3	3.1	−3.33	2.9	+3.33

Table 4

Comparison of estimated defect sizes (simulated) of circumferential bottom surface notches in mild-steel pipe obtained using phased array for various angles of inspection

Actual depth (mm)	Estimated depth (mm): $\theta = 30^\circ$ (%) error)	Estimated depth (mm): $\theta = 35^\circ$ (%) error)	Estimated depth (mm): $\theta = 40^\circ$ (%) error)	Estimated depth (mm): $\theta = 45^\circ$ (%) error)	Estimated depth (mm): $\theta = 50^\circ$ (%) error)	Estimated depth (mm): $\theta = 55^\circ$ (%) error)	Estimated depth (mm): $\theta = 60^\circ$ (%) error)
7	6.8 (+2.85)	6.8 (+2.85)	7.2 (−2.85)	7.2 (−2.85)	6.7 (+3.13)	7.2 (−2.85)	6.7 (+3.13)
5	5.1 (−2.0)	4.8 (+4.0)	5.1 (−2.0)	4.8 (+4.0)	5.2 (−4.0)	4.7 (+5.99)	5.3 (−5.99)
3	2.9 (+3.33)	2.8 (+6.66)	2.9 (+3.33)	3.1 (−3.33)	2.9 (+3.33)	2.8 (+6.66)	2.8 (+6.66)

Table 5

Comparison of estimated defect sizes (experimental) of circumferential bottom surface notches in mild-steel pipe obtained using phased array for various angles of inspection

Actual depth (mm)	Estimated depth (mm): $\theta = 30^\circ$ (%) error)	Estimated depth (mm): $\theta = 35^\circ$ (%) error)	Estimated depth (mm): $\theta = 40^\circ$ (%) error)	Estimated depth (mm): $\theta = 45^\circ$ (%) error)	Estimated depth (mm): $\theta = 50^\circ$ (%) error)	Estimated depth (mm): $\theta = 55^\circ$ (%) error)	Estimated depth (mm): $\theta = 60^\circ$ (%) error)
7	6.8 (+2.85)	6.7 (+3.13)	6.8 (+2.85)	6.7 (+3.13)	6.8 (+2.85)	6.8 (+2.85)	6.7 (+3.13)
5	4.8 (+4.0)	4.9 (+1.99)	4.8 (+4.0)	4.8 (+4.0)	4.7 (+5.99)	4.6 (+8.0)	4.5 (+10.0)
3	2.8 (+6.66)	2.8 (+6.66)	2.7 (+9.99)	2.8 (+6.66)	2.7 (+9.99)	2.6 (+13.33)	2.6 (+13.33)

phased array by steering the beam for an angular range of 30–60° at an angular increment of 5°. This variable angle steer can be easily and elegantly achieved by varying the focal law to steer the beam at the required angles, which would otherwise be a cumbersome procedure using a conventional transducer. Moreover, it is also possible to send a focused beam at different depths of foci in case of phased array to obtain a relatively clearer image of the defect when compared with a conventional transducer. The simulated and experimental sizes (estimated) of three bottom surface defects in the MS pipe specimen and the percentage errors are given in Tables 4 and 5, respectively, for three angles of inspection, and the corresponding simulated and experimental B-scan images indicating the corner trap and the tip diffracted signals are shown in Figs. 7–9.

It was observed that the separation between the corner trap and the tip diffracted echoes increased with the decrease in the inspection angle and a sufficient separation was achieved at angles 30° and 40°. Separation between the tip diffracted and the corner trap echoes is highly desirable when sizing small cracks. However, since the ultrasound path also increases or decreases with a corresponding

increase or decrease in the inspection angle, the probe has to be placed accordingly with respect to the defect position. A larger angle would mean that the probe should be placed at a larger distance away from the defect, which may be undesirable as it calls for a large scan length axis apart from having a low separation distance between the corner trap and the tip diffracted echoes. It was observed that for improved size estimation for small crack-like defects using L-wave, the angles 35–40° are recommended. Thus, it was inferred that operating at 35–40° angles of incidence was optimal for inspection using the RATT.

The simulation was then extended to study the imaging of inclined bottom surface cracks ($\pm 15^\circ$ with respect to the vertical) of 5 mm length in the 10-mm thick MS pipe specimen. The inclined crack B-scan images were compared with the B-scan image of the vertical bottom surface crack of similar dimensions. The simulated B-scan images of inclined bottom surface defects obtained for the 45° angle of inspection for the three configurations is given in Fig. 10. In the B-scan images, it was observed that the tip diffracted echo of the +15° inclined crack appears to the left while the tip diffracted echo of the −15° inclined crack appears to the right, when compared with the position of the tip

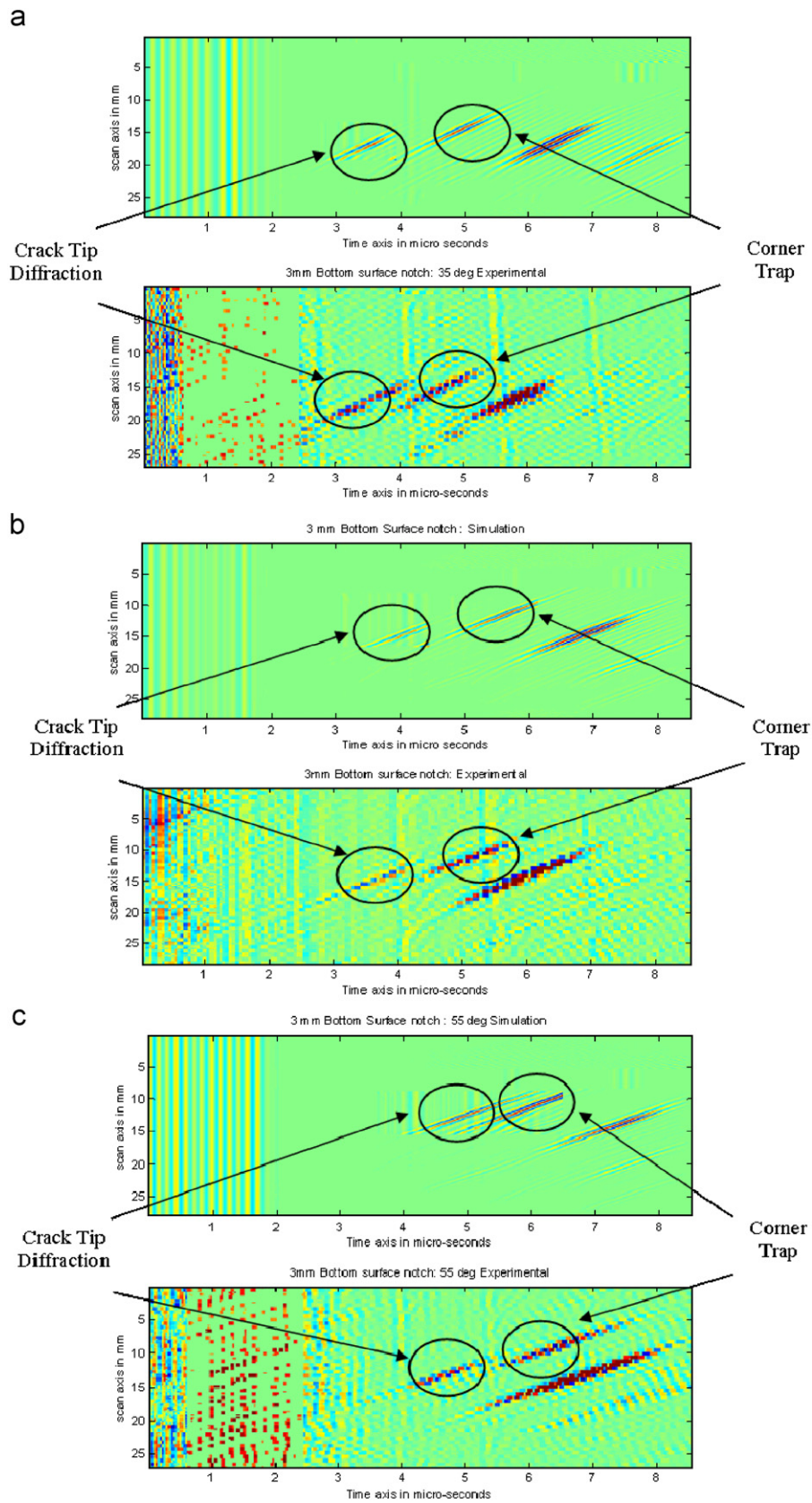


Fig. 7. Comparison of simulated and experimental B-scan images of 3-mm bottom surface crack obtained for the various angles of incidence. (a) 35°, (b) 45° and (c) 55° angle inspections: 3-mm bottom notches.

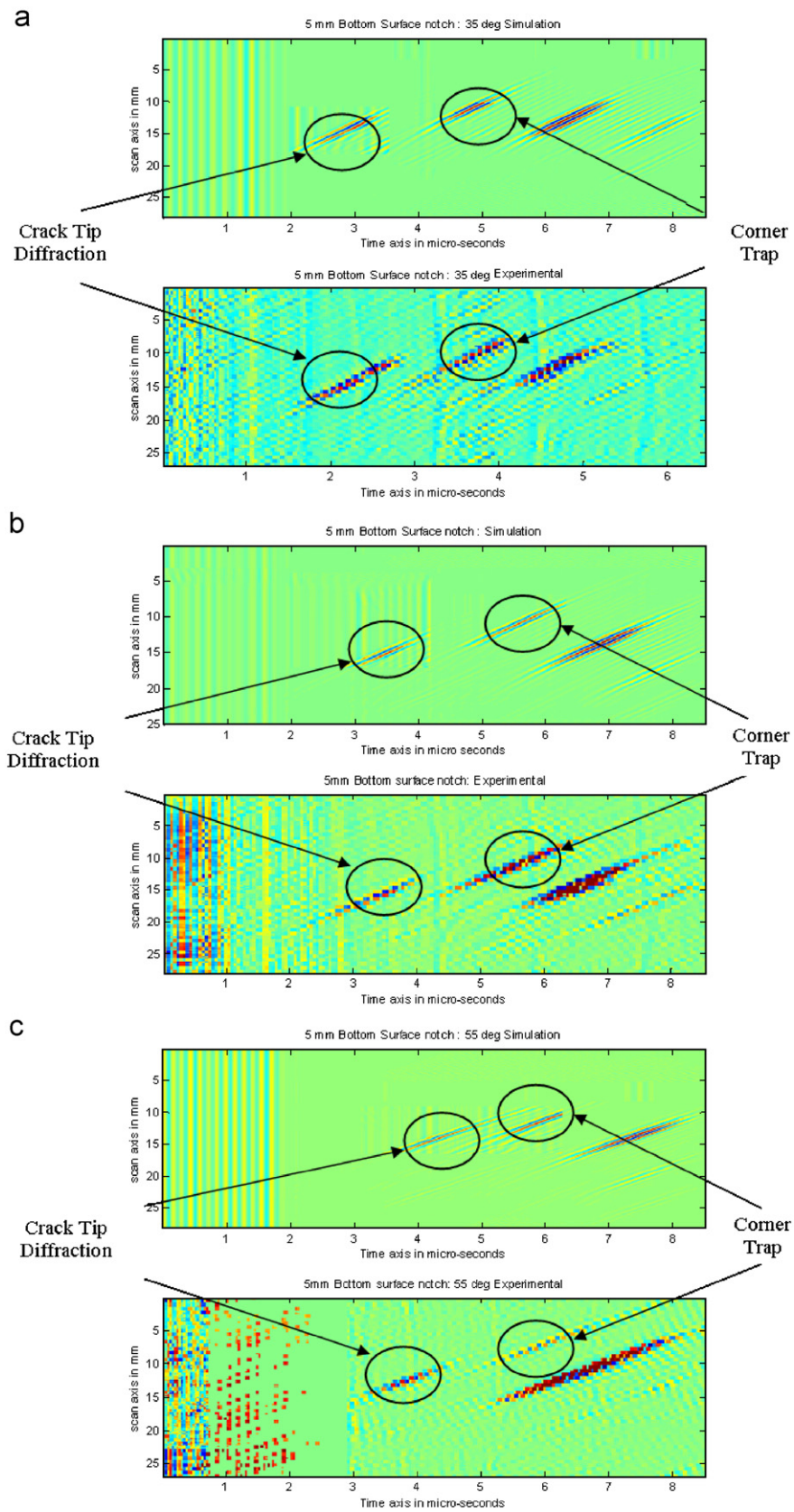


Fig. 8. Comparison of simulated and experimental B-scan images of 5-mm bottom surface crack obtained for the various angles of incidence. (a) 35° , (b) 45° and (c) 55° angle inspections: 5-mm bottom notches.

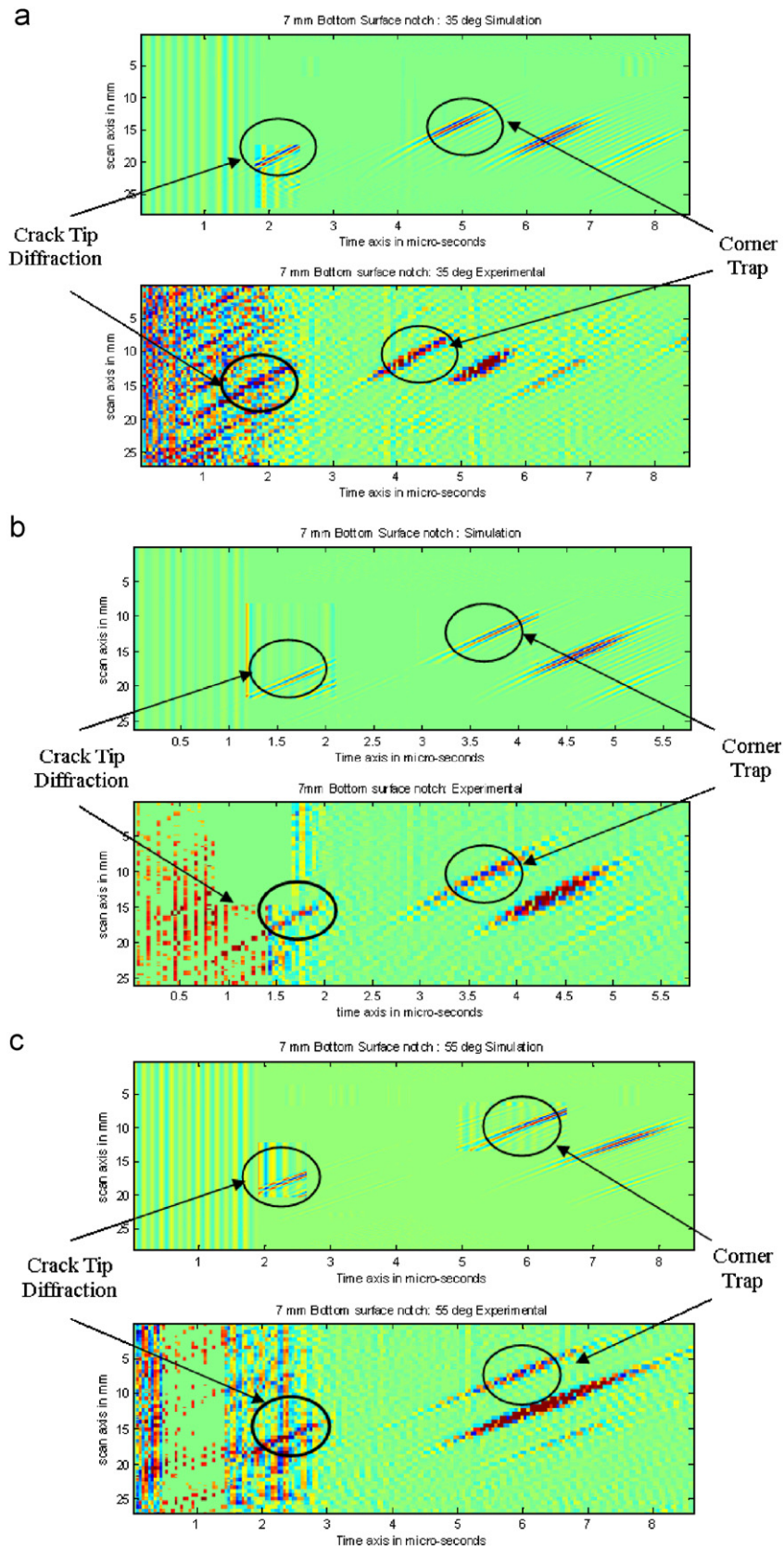


Fig. 9. Comparison of simulated and experimental B-scan images of 7-mm bottom surface crack obtained for the various angles of incidence. (a) 35°, (b) 45° and (c) 55° angle inspections: 7-mm bottom notches.

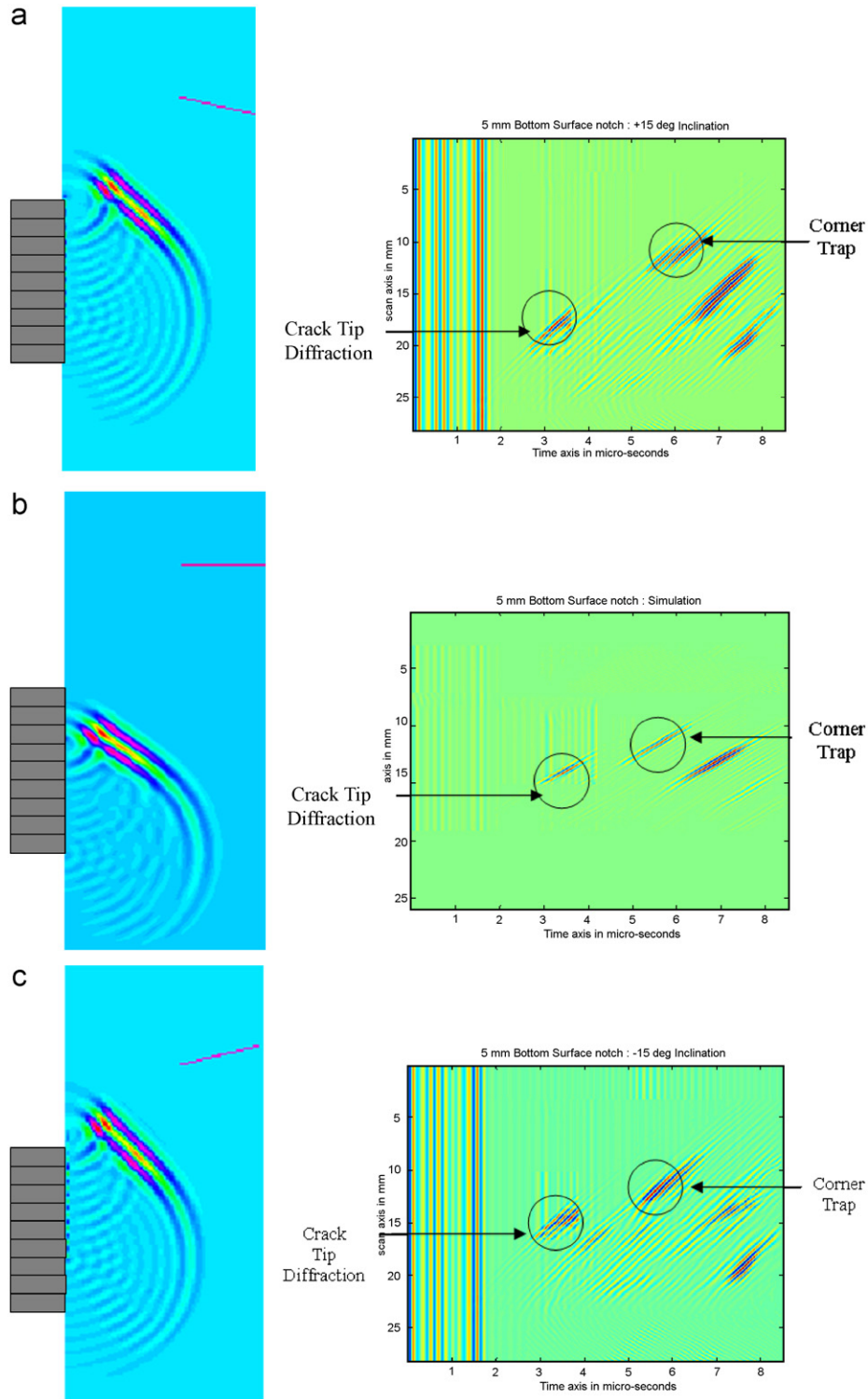


Fig. 10. Simulated B-scan image of inclined 5 mm bottom surface defects in the mild-steel pipe specimen obtained for the 45° angle of inspection. (a) +15° inclined, (b) 0° and (c) -15° inclined: 5-mm bottom surface notches.

diffracted echo of the vertical notch. Thus, it is inferred that the position of the tip diffracted echo relative to the corner trap position can be used as an indication to determine the inclination of the bottom surface crack using the phased array B-scan images.

6. Summary and conclusions

The simulation of phased array ultrasonic wave propagation and interaction with internal surface notches in a mild-steel pipe was studied. A 2D finite-difference time

domain model was successfully developed to simulate the phased array experiments on blocks and pipes and the simulation results were then compared with the experimental results. The results obtained from experiments validate the simulations. The simulated and the experimental B-scan data were used to size the defects and a comparison was made with the actual sizes of the defects. The 2D finite-difference time domain model developed in this study can also be used to study interaction of the ultrasonic waves with defects of various configurations and/or wave propagation in specimens with complex geometries. The model can thus be a useful tool in understanding signals that might otherwise be difficult to interpret in an experiment.

Ultrasonic testing of pipes is conventionally carried out using a 45°, 5 MHz (or 4 MHz) transducer. The effect of varying angles of inspection on the defect definition with regard to image clarity and size in the B-scan was also studied by steering the beam at the required angles using the phased array and it was inferred that when operating at lower inspection angles (35–40°), the tip diffracted and the corner trap echoes were well separated and, hence, it was more convenient to size the defects using the relative arrival time technique.

The imaging of inclined ($\pm 15^\circ$) bottom surface notches using the relative arrival time technique was carried out and it was inferred that the position of the tip diffracted echo can be used as an indication to determine the inclination of the notch.

References

- [1] Woodtli J, Kieselbach R. Damage due to hydrogen embrittlement and stress corrosion cracking. *Eng Failure Anal* 2000;7(6):427–50.
- [2] USNRC. An approach for plant specific, risk-informed decision making: in-service inspection of piping. Draft Regulatory Guide DG-1063. Washington, DC, US Nuclear Regulatory Commission: 1997.
- [3] Raj B, Mukhopadhyay CK, Jayakumar T. Frontiers in NDE research nearing maturity for exploitation to ensure structural integrity of pressure retaining components. *Int J Press Vessels Piping* 2006;83(5):322–35.
- [4] Rao BPC, Raj B, Jayakumar T, Kalyanasundaram P. An intelligent imaging scheme for automated eddy current testing. *NDT & E Int* 2000;17:41–57.
- [5] González DA, Madruga FJ, Quintela MA, López-Higuera JM. Defect assessment on radiant heaters using infrared thermography. *NDT & E Int* 2005;38(6):428–32.
- [6] Kalyanasundaram P, Raj B, Kasiviswanathan KV, Jayakumar T, Murthy CRL. Leak detection in pressure tubes of a pressurised heavy water reactor by acoustic emission technique. *Br J Nondestr Test* 1992;34:539–43.
- [7] Baskaran G, Balasubramanian K, Rao CL. Ultrasonic TOFD flaw sizing and imaging in thin plates using embedded signal identification technique (ESIT). *Insight—Non-Destructive Testing and Condition Monitoring* 2004;46:537–42.
- [8] Baby S, Balasubramanian T, Pardikar RJ, Jayakumar T, Rajkumar KV, Raj B. Sizing of cracks embedded in sub-cladding using the ultrasonic synthetic aperture focusing technique (SAFT). *Insight—Non-Destructive Testing and Condition Monitoring* 2004;46:26–30.
- [9] Satyanarayan L, Pukazhendhi DM, Balasubramanian K, Krishnamurthy CV, Murthy DSR. Phased array ultrasonic measurement of fatigue crack growth profiles in stainless steel pipes. *Int J Press Vessels Technol* 2007, in press.
- [10] Satyanarayan L, Mohan KV, Balasubramanian K, Krishnamurthy CV. Finite difference time domain simulation of ultrasonic phased array sector scan for imaging surface cracks in pipes, elbows and tee sections. *Res Nondestr Eval* 2007, in press.
- [11] Komura I, Hirasawa T, Nagai S, Takabayashi J, Naruse K. Crack detection and sizing technique by ultrasonic and electromagnetic methods. *Nucl Eng Des* 2001;206:351–62.
- [12] R/D Tech Guideline. Introduction to phased array ultrasonic technology applications. 1st ed. Canada: R/D Tech Inc.; 2004.
- [13] R/D Tech's Technology Information. Ultrasound phased array. *J Nondestr Test* 2002;7(5) <<http://www.ndt.net/article/v07n05/rdtech/rdtech.htm>>.
- [14] Poguét J, Marguet J, Pichonnet F, Chupin L. Phased array technology: concepts, probes and applications. *J Nondestr Test* 2002;7(5) <<http://www.ndt.net/article/v07n05/poguét/poguét.htm>>.
- [15] Vanhille C, Conde C, Campos-Pozuelo C. Finite-difference and finite-volume methods for nonlinear standing ultrasonic waves in fluid media. *Ultrasonics* 2004;42(1–9):315–8.
- [16] Schroder CT, Scott Jr WR. A finite difference model to study the elastic wave interactions with buried land mines. *IEEE Trans Geosci Remote Sensing* 2000;38(4):1505–12.
- [17] Pörtzgen N, Volker AWF, Fingerhut M, Tomar M, Wassink C. Finite difference simulation of ultrasonic NDE methods for the detection and sizing of Stress Corrosion Cracking (SCC). *AIP Conf Proc* 2005;820:1902–9.
- [18] Hastings D, Schneider JB, Broschat SL. Application of the perfectly matched layer (PML) absorbing boundary condition to elastic wave propagation. *J Acoust Soc Am* 1996;100:3061–8.
- [19] Azar L, Shi Y, Wooh SC. Beam focusing behavior of linear phased arrays. *NDT & E Int* 2000;33(3):189–98.
- [20] Ciorau P. Contribution to detection and sizing linear defects by conventional and phased array ultrasonic techniques. *J Nondestr Test* 2005;10(9) <www.ndt.net/article/wcndt2004/pdf/power_generation/233_ciorau.pdf>.
- [21] Anderson MT, Cumblidge SE, Doctor SR. Through weld inspection of wrought stainless steel piping using phased array ultrasonic probes. In: 16th WCNDT 2004—world conference on NDT, Montreal, Canada. <www.ndt.net/article/wcndt2004/pdf/array_transducers/460_anderson.pdf>.
- [22] Davis JM. Advanced ultrasonic flaw sizing handbook. *J Nondestr Test* 1998;3(11) <<http://www.ndt.net/article/1198/davis/davis2.htm>>.
- [23] Wüstenberg H, Erhard A. Approximative modeling for the practical application at ultrasonic inspections. *J Nondestr Test* 1997;2(5) <<http://www.ndt.net/article/wsho0597/wuesten2/wuesten2.htm>>.